NANO · MICRO small
www.small-journal.com

Template-Directed Polymerization of Binary Acrylate Monomers on Surface-Activated Lignin Nanoparticles in Toughening of Bio-Latex Films

Luyao Wang, Qingbo Wang, Emil Rosqvist, Jan-Henrik Smått, Qiwen Yong, Lippo Lassila, Jouko Peltonen, Thomas Rosenau, Martti Toivakka, Stefan Willför, Patrik Eklund, Chunlin Xu, and Xiaoju Wang**

Fabricating bio-latex colloids with core–shell nanostructure is an effective method for obtaining films with enhanced mechanical characteristics. Nano-sized lignin is rising as a class of sustainable nanomaterials that can be incorporated into latex colloids. Fundamental knowledge of the correlation between surface chemistry of lignin nanoparticles (LNPs) and integration efficiency in latex colloids and from it thermally processed latex films are scarce. Here, an approach to integrate self-assembled nanospheres of allylated lignin as the surface-activated cores in a seeded free-radical emulsion copolymerization of butyl acrylate and methyl methacrylate is proposed. The interfacial-modulating function on allylated LNPs regulates the emulsion polymerization and it successfully produces a multi-energy dissipative latex film structure containing a lignin-dominated core (16% dry weight basis). At an optimized allyl-terminated surface functionality of 1.04 mmol g^{-1}, the LNPs-integrated latex film exhibits extremely high toughness value above 57.7 MJ m^{-3}. With multiple morphological and microstructural characterizations, the well-ordered packing of latex colloids under the nanoconfinement of LNPs in the latex films is revealed. It is concluded that the surface chemistry metrics of colloidal cores in terms of the abundance of polymerization-modulating anchors and their accessibility have a delicate control over the structural evolution of core–shell latex colloids.

1. Introduction

Latex colloids have prevailed as ideal materials across a wide range of film and binding applications, ranging from simple coatings and binders, to structurally colored materials and advanced functional templates, such as porous supraparticles and complex crystal superstructures, due to their facile surface functionalization and tunable colloidal assembly.[1–6] Films fabricated from latex colloids with a unique core–shell morphology is a novel class of nanoparticle-polymer composites that synergistically integrate the versatility of nanoparticles (core) with the processability and diversity of the corona polymers (shell).[5,7] Two techniques, that is, seeded free-radical emulsion polymerization and controlled radical emulsion polymerization of amphiphilic block copolymers (commonly a macro chain-transfer agent), have proven effective in devising multifunctional core–shell latex colloids.[7–9] In the above-mentioned techniques, the seed of the latex colloid or the hydrophobic core that is derived from the polymerization-induced self-assembly in aqueous dispersion functions as an interfacial modulator to direct hydrophobic polymer growth on the core surface or in the core, respectively.[10,11] Compared with controlled radical emulsion polymerization, seeded emulsion polymerization offers more possibilities to vary the constituents of the core (e.g., polyesters, polyolefins, polyvinyl acetate,

L. Wang, Q. Wang, Q. Yong, T. Rosenau, M. Toivakka, S. Willför, C. Xu, X. Wang
Laboratory of Natural Materials Technology
Åbo Akademi University
Henrikinkatu 2, Turku FI-20500, Finland
E-mail: Chunlin.Xu@abo.fi; xwang@abo.fi

The ORCID identification number(s) for the author(s) of this article can be found under https://doi.org/10.1002/smll.202207085.

DOI: 10.1002/smll.202207085

E. Rosqvist, J.-H. Smått, J. Peltonen
Physical Chemistry
Laboratory of Molecular Science and Engineering
Åbo Akademi University
Henrikinkatu 2, Turku FI-20500, Finland
L. Lassila
Turku Clinical Biomaterials Centre
University of Turku
Itäinen Pitkäkatu 4b, Turku FI-20520, Finland
T. Rosenau
Department of Chemistry
University of Natural Resources and Life Sciences Vienna (BOKU University)
Konrad-Lorenz-Strasse 24, Tulln AT-3430, Austria
P. Eklund
Organic Chemistry
Laboratory of Molecular Science and Engineering
Åbo Akademi University
Henrikinkatu 2, Turku FI-20500, Finland

acrylics, polysaccharides, silica) and distinct shell geometries, such as raspberry- and dumbbell-like features, can be fabricated on the seed.[5,8,11–16] Nevertheless, the major obstacles in conferring the desired properties to such nanoparticle-polymer composites via seeded emulsion polymerization are their interfacial compatibility at molecular level (i.e., surface recognition of hydrophobic monomers during emulsion polymerization) and state of dispersion on the nanoscale. Extensive research has been devoted to understanding the mechanism and kinetics of core–shell emulsion polymerization, interfacial behavior of the core polymer in latex colloids (e.g., surface functionality and/or surface wettability), and the consequent role that it plays in determining the physiochemical properties of these nanocomposites when forming a thin film.[7,9,10,15,17] On the basis of these studies, a variety of strategies have therefore been implemented, such as utilizing nanoparticle surface-grafting chemistry and devising multi-energy dissipative structures enriched with strong and recoverable sacrificial bonds.[15,18–20] These approaches can enhance the surface compatibility of core–shell colloids and improve the dispersion state of latex. However, it is yet still a challenge to uniformly arrange the polymerization-active sites on the nanoparticle core surface and to simultaneously fine-tune its physiochemical properties (e.g., functionalities, particle size, thermal properties) in a green and facile fabrication route.

The film formation properties of latex colloids strongly rely on different phases of thermal annealing, such as colloidal re-arrangement, interparticle chain-diffusion, and colloid coalescence.[21,22] Film toughness, one of the crucial metrics for assessing latex applications, usually depends on the mechanical strength of the individual latex colloids and the entanglement of polymer chains, which is the fundamental mechanism behind high toughness in bulk polymers.[23–26] One of the recent developments to improve the toughness of latex film is the use of flexible crosslinkers. Aoki et al. synthesized macromolecular rotaxane, consisting of a polymer chain threading into a crown ether with one vinyl group per component.[25] Hiroshige et al. and Kureha et al. successfully fabricated poly(butyl acrylate-*co*-methyl methacrylate) (pBM) latex colloids crosslinked by rotaxane, wherein the stress relaxation in each colloid that originated from the flexibility of the crosslinking points toughened the latex film.[24,26] The increased polymer chain entanglement density and energy dissipation capacity observed in poly(methyl acrylate) grafted silicon dioxide nanoparticle composite has been reported for impact mitigation application.[27] However, polymer chain disentanglement and reduced tensile modulus were also observed in acrylic coatings with physically associating nano-titanium dioxide single units since the polymer chain interplays and conformation can be modulated under the spatial confinement of nanoparticles.[28] Therefore, rather than the specific polymer chemistry, the impact of nanoparticles on polymer chain dynamics during film formation, including interdiffusion, entanglement, and nanoconfinement, should play a predominant role in the construction of high-performing nanoparticle-polymer latex materials. In the emerging cases of core–shell surface-interacted latex colloids, the complex nanostructure raises a need to better understand the role of the core-stimulated film morphology (e.g., packing manner of latex colloids, core–shell boundary interaction) in the resulting performance.

The environmental consciousness in society is shifting the focus toward the use of bio-based, green products and sustainable processes. The need to replace petroleum-based chemistries with renewable bio-based raw materials is also trending in the production of latex. This quest for improving sustainability has led to exploring hemicelluloses-,[12] starch-,[29] or lignin-functionalized latex colloids.[30] For instance, pBM latex produced by in situ seeded semi-batch emulsion polymerization of butyl acrylate (BA) and methyl methacrylate (MMA) using 1.0 wt% maleoylated lignin as the seed exhibited enhanced tack and shear strength that supported their use in pressure-sensitive adhesive applications.[30] Lignin, the most abundant aromatic bioresource, also has a unique nanotechnological advantage—nanospheres of lignin possess durable dispersibility in water and certain organic solvents, which allows for free-radical emulsion polymerization of lignin with water-immiscible monomers in water medium.[31,32] It has previously been demonstrated that the surface of lignin nanoparticles (LNPs) can mediate the polymerization process and generate energy dissipative interactions with entangled polymer chains in toughening cellulose-polycaprolactone nanocomposites, polystyrene (PSt), poly(vinyl alcohol), pectin-polyacrylic acid hydrogels, etc.[33–36] Moreover, the presence of multi-functional groups in lignin, such as phenolic hydroxyls (phenolic-OH) and aliphatic hydroxyls (aliphatic-OH), facilitates the application-specific functionalization of it. For instance, lignin derivatives functionalized via phenolic-OH with bromopropionyl group and xanthate can be utilized as macroinitiators for atom transfer radical polymerization and as macromolecular chain-transfer (macro-CT) agents for reversible addition-fragmentation transfer (RAFT) polymerization, respectively.[37,38] Furthermore, among the different chemical modifications of lignin, allyl-terminated polymers characterized by the presence of a double bond enable the fabrication of diverse architectures and functionalities through post-modifications, for example, thiol-ene click chemistry,[39,40] epoxidation,[41] photo-induced crosslinking,[42] free-radical polymerization.[43,44]

Herein, a new class of aqueous bio-latex colloids (A-LNP-pBM) composed of an allylated LNPs (A-LNPs) core and a pBM acrylate polymer shell from seeded emulsion polymerization is developed and their molecular interface properties (i.e., surface functionality and hydrophobic monomer conversions) and physicochemical behavior of nanostructures are studied. Thermally dried and annealed bio-latex films are investigated in terms of nanoparticle (core)-stimulated morphology using small-angle X-ray scattering (SAXS) and scanning electron microscope (SEM) and correlated to quantitative nanomechanical atomic force microscopy (AFM) measurements. The observed phenomena in core–shell boundary coalescence during film formation combined with the as-measured mechanical characteristics are used to systematically correlate the effect of morphology on the toughness of latex film. To clarify the above-mentioned correlation, we emphasize the tunability of colloidal cores in terms of the abundance of polymerization-active anchors and their accessibility, which emerge as important factors that have a delicate control over the structural evolution of core–shell latex colloids. In this study, the investigation of bio-latex colloids at the molecular level and material characterizations on nano- as well as micro-scales enable tailoring of the morphology and resulting mechanical characteristics for high-end applications.

2. Results and Discussion

2.1. Fabrication Rationale of a Tough Bio-Latex Film

Our approach to fabricate surface-functionalized LNPs as a structural template for directing emulsion polymerization of acrylate monomers starts with the preparation of allylated lignin via base-catalyzed etherification of lignin hydroxyl groups with oxirane groups from allyl glycidyl ether (**Figure 1**a). Birch alkaline lignin fractionated by isopropyl alcohol (birch-*i*-PrOH) was used for allylation reaction. Next, the hydrophobic self-assembly of the allylated lignin macromolecules in water conveniently occurs when the anionic groups are protonated as the pH is decreased in the purifying dialysis process, resulting in the formation of a dispersion of A-LNPs (Figure 1b). The allyl groups distributed on the surface of A-LNPs can serve as the polymerization-active anchors to further modulate the emulsion polymerization of binary monomers (e.g., BA and MMA mixture) in terms of the monomer transport and conversion (Figure 1c). When the core–shell latex colloids are thermally dried and annealed at a temperature above their glass transition temperature (Tg), film formation is initiated, which is characterized by two stages, that is, latex colloids deformation and polymer chain interdiffusion (Figure 1d). It is hypothesized that the high-volume fraction and small size of A-LNPs together with different content of surface functionalities can lead to chemical tuning and physical confinement of the acrylate polymers. Moreover, the tunability of the physiochemical properties of the A-LNP-pBM latex nanospheres can facilitate the control over the core–shell boundary coalescence and polymer chain interdiffusion between the latex colloids, which is expected to be effective in improving the polymer dispersion and toughening of the bio-latex films.[45]

2.2. Tunability of Physicochemical Properties of the A-LNPs

The degree of substitution (DS) of allyl groups was varied using predetermined 1.0, 1.5, 2.5, and 4.0 molar ratios of allyl glycidyl ether relative to the content of hydroxyl groups present in lignin (4.71 mmol g^{-1}, **Table 1**). Four homogeneous A-LNPs dispersions with pH around 5.5 were obtained after dialyzing the resulting solution of the allylated lignin (pH 12) against distilled water, as shown in **Figure 2**a. The details of the preparation parameters and final yields of the A-LNPs are summarized in Table S1, Supporting Information. The lignin allylation process was revealed by quantitative ^{31}P NMR spectroscopy. As noted in Figure 2b, a decreasing signal of phenolic-OH groups, concomitant with a newly formed and an increasing aliphatic-OH signal at $\sigma = 146.27$ ppm, suggests that the proposed lignin allylation procedure is mainly selective to convert lignin phenolic-OH to allyl aryl ethers in the presence of other lignin functionalities, that is, aliphatic-OH and carboxylic acid (COOH). The formation of lignin self-assembly as nanospheres is evident from the transmission electron microscopy (TEM) imaging, and the contrast differences present on individual A-LNPs seem to support our hypothesis that the allyl-terminated polymer chains can assemble on the particle surface via pH-trigger mechanism

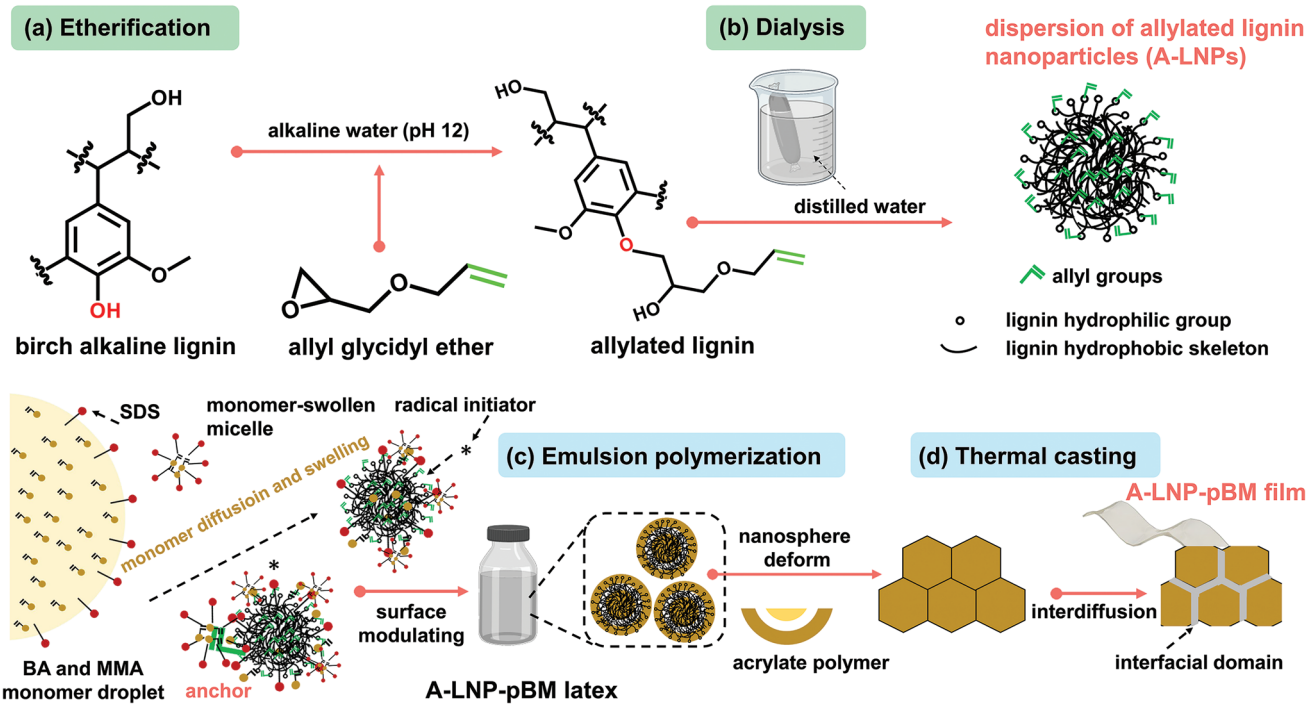

Figure 1. Design strategy for the surface-functionalized LNPs and tough bio-latex films: a,b) preparation of A-LNPs dispersion by functionalization of lignin with allyl-terminated groups via anionic ring-opening reaction under alkaline conditions followed by dialysis. c,d) Fabrication of A-LNP-pBM latex colloids by the seeded free-radical emulsion polymerization of BA and MMA using A-LNPs as a structural template in aqueous media followed by film formation using thermal casting.

Table 1. Hydroxyl and allyl group distributions (mmol g^{-1}) in A-LNPs and birch-*i*-PrOH sample according to quantitative ^{31}P NMR and ^{1}H NMR, respectively.

Samples	Aliphatic-OH	Phenolic-OH	—COOH	Total OH	Allyl groups[a)]	DS(A)[b)]
Birch-*i*-PrOH	0.86	2.88	0.97	4.71	–[c)]	–[c)]
A-LNP-1.0	2.56	1.38	0.25	4.19	0.31	2.15
A-LNP-1.5	2.99	0.72	0.32	4.03	0.57	2.35
A-LNP-2.5	3.04	0.54	0.48	4.06	1.04	2.61
A-LNP-4.0	3.08	0.32	0.38	3.78	1.23	2.80

[a)]Quantified by ^{1}H NMR (298 K, 500.13 MHz, D_2O) using 3-(trimethylsilyl) propionic-2,2,3,3-d_4 acid, sodium salt as internal standard; [b)]Quantified by ^{1}H NMR (298 K, 500.13 MHz, DMSO-d_6) using 4-nitrobenzaldehyde as internal standard; [c)]Denotes not detectable.

during dialysis, as indicated by red arrows in Figure 2a. The ^{1}H NMR method reported by Pylypchuk et al., that is, NMR pulse sequence combining pre-saturation and excitation sculpting water suppression, was successfully applied to evaluate the surface composition of LNPs in aqueous dispersion.[46] The above-mentioned ^{1}H NMR method was also applied in this work and the aqueous ^{1}H NMR spectra indeed confirmed the presence of allyl aryl ethers on the A-LNPs (Figure 2c), as indicated by the signals ascribed to allyl groups at $\sigma = 5.89$ ppm. Furthermore, the integral from 5.80 to 6.00 ppm was used as an empirical metric to denote the surface functionality of A-LNPs, that is, allyl groups assembled on the surface of A-LNPs, as listed in Table 1. In the meantime, the DS of allyl groups (DS(A)) on lignin macromolecules were quantified by ^{1}H NMR in dimethyl sulfoxide-d_6 (DMSO-d_6) solution. It was found that the surface functionality of A-LNPs increased from 0.31 to 1.23 mmol g^{-1} as the DS(A) increased from 2.15 to 2.80 mmol g^{-1} (see details in Figure S1, Supporting Information). In the meantime, high-resolution X-ray photoelectron spectroscopy (XPS) spectra of C 1s corroborate the formation of allyl-terminated chains (—C=C—) in the near-surface layer of the A-LNPs (Figure S2 and Table S2, Supporting Information). A fine control over the physicochemical properties of A-LNPs in terms of particle size and Tg was also achieved. More specifically, the lignin macromolecules in higher allylation degrees favored the formation of small-size A-LNPs (e.g., particle size decreased from 225 to 150 nm) with low Tg values. Considering the effect of the degree of allylation on the ratio of aliphatic-OH/phenolic-OH content, the observed particle size variation of A-LNPs is consistent with the results reported by Morsali et al., where smaller LNPs were obtained when increasing the content of surface-distributed aliphatic-OH groups by ring-opening of cationic epoxides.[32] The main

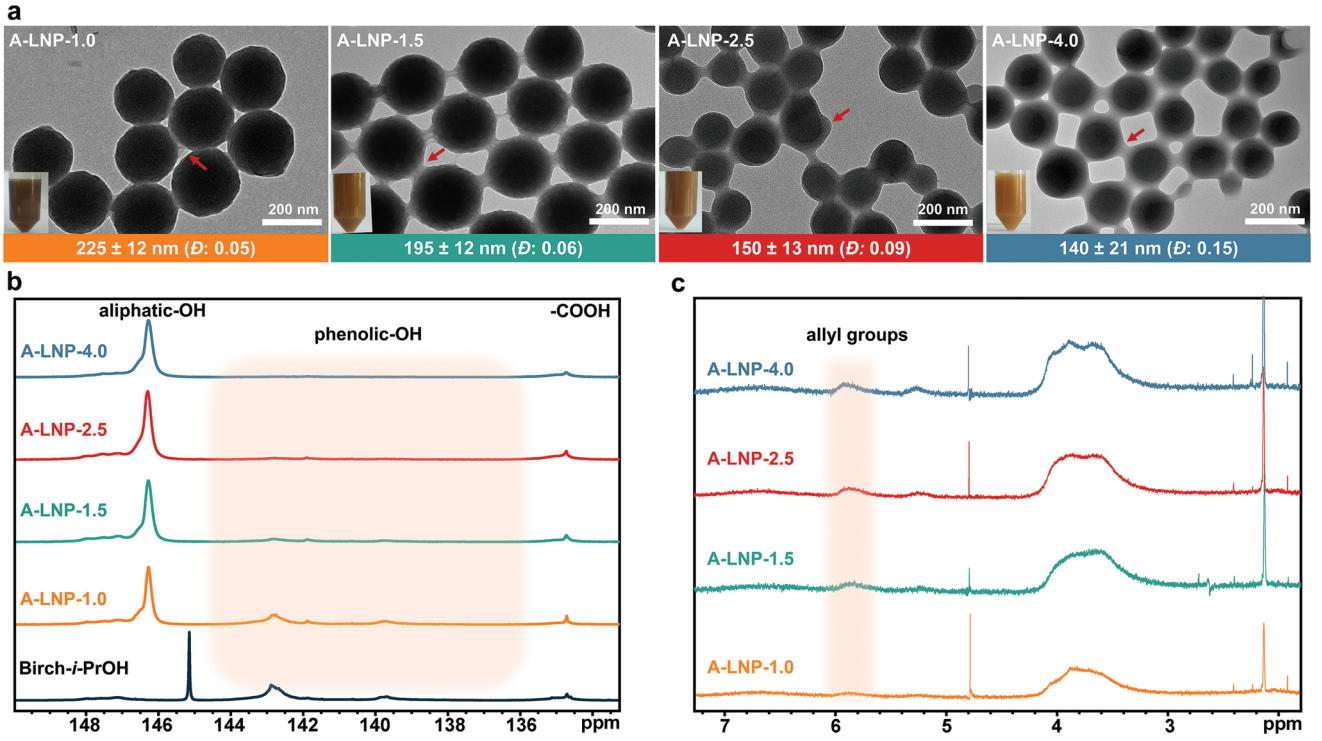

Figure 2. Nanostructure of A-LNPs and their functionality at the molecular scale. a) TEM images of A-LNPs. The insets in (a) are digital photographs of the corresponding A-LNPs dispersions. b) Quantitative ^{31}P NMR spectra of A-LNPs. c) ^{1}H NMR spectra of A-LNPs in D_2O demonstrating surface functionalization.

mechanism for the formation of A-LNPs is the protonation of the ionized hydroxyl groups of lignin macromolecules to trigger self-assembly with its surrounding molecules. The aliphatic-OH/phenolic-OH content dictates the ease of allylated-lignin nucleation since the ionized aliphatic-OH groups are susceptible to protonation due to their higher p*K*a values than that of phenolic-OH groups.[47] This explains the decreasing size of A-LNPs as the increase of aliphatic-OH/phenolic-OH content. Also, the lower surface tension of lignin macromolecules in a higher allylation degree probably supports the size difference of A-LNPs since the lower cohesion between neighboring molecules can facilitate the formation of smaller-sized lignin nanospheres (Table S3, Supporting Information). The Tg of A-LNPs decreased from 125 °C of birch-*i*-PrOH sample to 80 °C of A-LNP-1.0 following 57 °C of A-LNP-1.5 and 48 °C of A-LNP-2.5, as seen in the differential scanning calorimetry (DSC) thermograms (Figure S3a, Supporting Information). This strongly indicates that the allylation degree can tune the domain flexibility of polymerization-active anchors on LNPs. In addition, the surface wettability of A-LNPs was observed to be dependent on the allylation degree, where the water contact angle (WCA) increased from 26.6° of A-LNP-1.0 to 43.6° of A-LNP-2.5 sample (Figure S3b, Supporting Information). These characteristics are highly relevant metrics for the use of A-LNPs as a structural template in core–shell emulsion polymerization of hydrophobic monomers where the accessibility of the core surface can yield a significant difference by the abundance of surface functionality, the ease of polymer chain conformation, and surface hydrophobicity (Figure 1c). It is worth noting that A-LNP-4.0 exhibited a Tg transition at 77 °C and a WCA value of 34.3°, indicating the recalcitrance of lignin macromolecules very possibly due to excessive entanglement of allyl-terminated chains.

2.3. Free-Radical Emulsion Polymerization of Acrylate Monomers in the Presence of A-LNPs as a Structural Template

The bio-latex system is produced by free-radical emulsion polymerization of water-immiscible acrylate monomers in a A-LNPs water dispersion using sodium dodecyl sulfate (SDS) as the emulsifier and ammonium persulfate (APS) as the free-radical initiator (**Figure 3**a). The spherical nanostructures of pBM and A-LNP-pBM latex colloids are evident in the TEM images obtained by using the uranyl acetate negative staining method (Figure 3b,d,f,h). As illustrated in the TEM image of A-LNP-1.0-pBM and its corresponding histograms of size distribution (Figure S4, Supporting Information), small domains of pBM homopolymer with sizes of 25–50 nm were present on A-LNPs, indicating the surface-initiated covalent polymerization. It is noteworthy that, when the LNPs with more surface allyl groups, higher surface hydrophobicity, and lower Tg values than A-LNP-1.0 were used as the polymerization templates, A-LNP-pBM latex colloids presented a concentric core–shell morphology. The size distribution histograms and dispersity ($Đ$) values confirm a relatively uniform particle size ($0.06 < Đ < 0.17$) for most of the prepared A-LNP-pBM colloids without any evidence of free LNPs in the dispersion, with the exception of A-LNP-1.5-pBM (Figure 3d). In the present synthesis, the size of the A-LNP-pBM latex particles is dependent on the surface functionality of A-LNPs, wherein an increase in the content of surface-distributed allyl groups from 0.57 to 1.23 mmol g^{-1} was observed to lead to a significant decrease in the average size of the A-LNP-pBM, from 141 to ≈91 nm. We confer that the size of the A-LNP-pBM decreased with the increased content of allyl groups could be attributed to two factors. First, the average A-LNP core size decreased with increasing the surface functionality in the order A-LNP-1.0 (225 nm) > A-LNP-1.5 (195 nm) > A-LNP-2.5 (150 nm) > A-LNP-4.0 (140 nm). Second, the A-LNPs core with lower Tg values and higher content of polymerization-active anchors can facilitate the covalent interpenetration with the shell of acrylate polymer during emulsion polymerization, which may possibly result in smaller A-LNP-pBM latex colloids.

From the perspective of chemical composition, the ^{1}H NMR spectra of A-LNP-pBM identified the formation of pBM copolymers (Figure S5, Supporting Information), while the extent of interfacial compatibility between A-LNPs and acrylate monomers was determined using high-performance liquid chromatography (HPLC). For example, the quantitative monomer conversion kinetic curves for emulsion polymerization of BA and MMA in the presence of A-LNPs were monitored as a function of reaction time (see details of monomer calibration curves in Supporting Information). As shown in Figure 3j, 95 wt% of MMA and 88 wt% of BA were integrated into the A-LNP-2.5-pBM copolymer after monomer addition (0–1 h), while almost all the acrylate monomers were polymerized when the reaction time was prolonged to 6 h. In addition, there was a change in the color of the A-LNP-2.5-pBM emulsion from brownish to milky yellowish, indicating the high coverage of pBM shell on A-LNP core (see insets in Figure 3j). These results validate the feasibility of using A-LNPs as core–shell emulsion polymerization templates in achieving ideal shell polymer composition with high efficacy. The monomer conversion rate increased in the order of A-LNP-1.0-pBM (56.5%) < A-LNP-1.5-pBM (90.7%) < A-LNP-4.0-pBM (97.3%) < A-LNP-2.5-pBM (100%), as shown in Table S4 and Figure S6, Supporting Information. It should be noted here that the monomer conversion rate of BA was much less pronounced than that observed for MMA and only residual BA was identified by HPLC chromatogram in both the pBM and A-LNP-pBM latex emulsions (Figure S6, Supporting Information). This can be attributed to the higher monomer diffusion rate in water medium or the intrinsic higher polymerization rate of MMA.[48] Since the A-LNP-1.0-pBM and A-LNP-1.5-pBM latex emulsions had much more BA residues than the neat pBM, it is inferred that A-LNPs with a low content of surface polymerization-active anchors can deteriorate the emulsion polymerization process and drift the shell polymer composition of pBM toward the reactive monomer as the degree of conversion increases. One should note that while A-LNP-4.0 nanospheres, when compared to A-LNP-2.5-pBM, had a higher surface allyl group content than A-LNP-2.5, the higher Tg and lower WCA values still resulted in a latex emulsion with a higher BA residue content. Therefore, the results support the hypothesis that the BA and MMA monomers can recognize the molecular-scale differences on A-LNPs that depend not only on the abundance of the allyl-terminated anchors but also on their sufficient domain flexibility and surface hydrophobicity, which

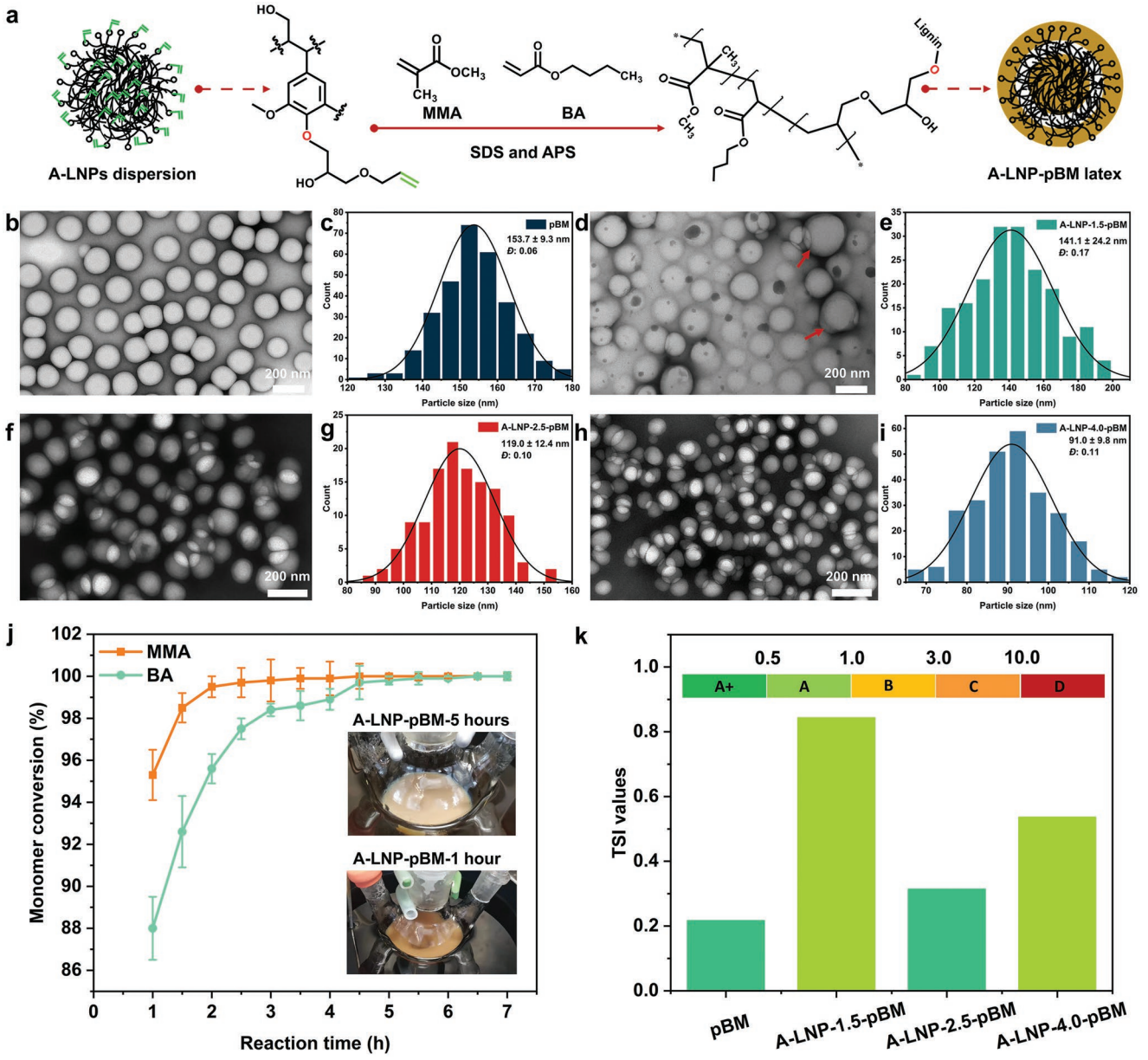

Figure 3. Evaluation of the impact of A-LNPs with varying content of surface functionalities on the performance of emulsion polymerization of BA and MMA monomers. a) Schematic illustration for the preparation of A-LNP-pBM latex colloids. The structure of A-LNP-pBM polymer is only for conceptual demonstration. TEM images of b) pBM, d) A-LNP-1.5-pBM, f) A-LNP-2.5-pBM, h) A-LNP-4.0-pBM, and their c,e,g,i) particle size distribution histograms. Individual lignin nanoparticles in A-LNP-1.5-pBM are indicated by red arrows. j) Kinetic plots showing monomer conversion for the emulsion copolymerization of BA and MMA with A-LNP-2.5. The insets in (j) are photographs of A-LNP-2.5-pBM latex at two time-points. k) Global TSI histogram of pBM and A-LNP-pBM latex at 12 h. The inset in (k) is the TSI scale to assess emulsion destabilization.

result in improved accessibility to the core in the core–shell emulsion polymerization. The coagulum formation related to the destabilization of pBM and A-LNP-pBM latex was monitored by the turbiscan stability index (TSI). As seen in Figure 3k, the TSI values of A-LNP-pBM latex within 12 h were slightly higher than those of the neat pBM, indicating comparatively lower stability of the former, yet maintaining in a good level of stability (A^+ or A) according to the TSI color scale (see insets in Figure 3k). In addition, the pBM and A-LNP-pBM latex colloids were highly negatively charged, ranging from −55 to −75 mV, which could stabilize the latex emulsion via electrostatic repulsion.

2.4. Morphology of A-LNPs-Based Stretchable pBM Bio-Latex Films

Self-standing, dense, crack-free, and stretchable pBM and A-LNP-pBM films were obtained by evaporating water from the latex emulsions and annealing at 50 °C (**Figure 4**a).

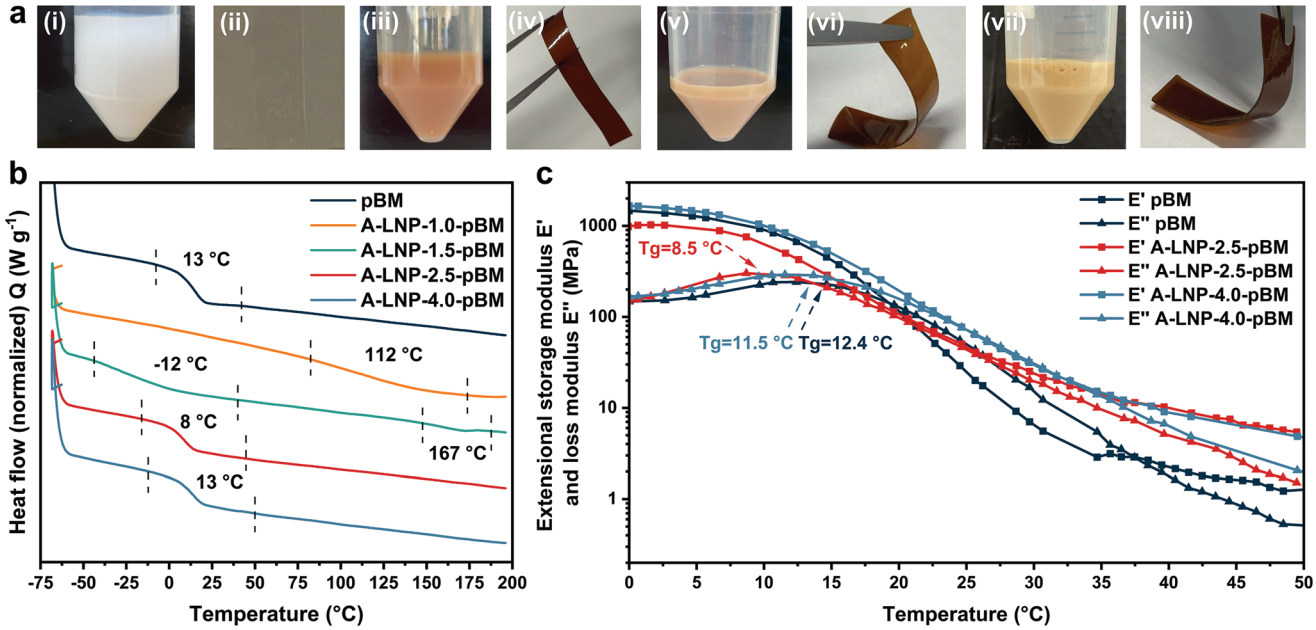

Figure 4. Thermal and mechanical properties of latex films. a) Images of latex emulsions before coalescence and after film formation for i,ii) neat pBM, iii,iv) A-LNP-1.5-pBM, v,vi) A-LNP-2.5-pBM, and vii,viii) A-LNP-4.0-pBM, respectively. b) DSC curves of latex colloids showing the Tg, which was identified by the midpoint of the thermal transition region. c) Temperature-dependent functions of extensional E′ and E″ for neat pBM and A-LNP-pBM latex films, where Tg was identified by the peak in E″.

Subsequently, the key thermal parameters for latex film formation, such as Tg, were investigated by DSC measurements, shown in Figure 4b. Compared with the Tg of random pBM copolymer at 13 °C, the decrease in Tg with decreasing content of polymerization-active anchors on A-LNPs in the order A-LNP-4.0-pBM (13 °C) > A-LNP-2.5-pBM (8 °C) > A-LNP-1.5-pBM (–12 °C) is clearly visible. Most notably, the A-LNP-4.0-pBM latex colloids exhibited a similar Tg value as pBM, while the A-LNP-1.5-pBM latex colloids possessed extremely low Tg value of –12 °C. It is expected that the polymer chain of pBM would be covalently polymerized and confined with A-LNP-4.0 nanospheres owing to the largest content of surface allyl groups (i.e., 1.23 mmol g^{-1}). In other words, the pBM polymer shell is repelled from the A-LNP interface induced by reduced covalent surface interactions (e.g., 0.57 mmol g^{-1} allyl groups in A-LNP-1.5), leading to an enhanced segmental mobility and hence overall decrease in Tg.[49] It should be noted here that an obscure Tg region at 167 °C also appeared in the thermogram of A-LNP-1.5-pBM, which can originate from the individual A-LNP-1.5 in the latex. In the most extreme case, the A-LNP-1.0-pBM latex colloids exhibited only one ambiguous Tg at 112 °C and were not able to create continuous films, which strongly indicate that A-LNP-pBM without core–shell nanostructure is present in the form of nanofiller and severely interferes with the film formation (Figure S7, Supporting Information). In addition, it is also confirmed that the formation of smooth and flexible latex films depended on the deformability of the latex colloids (i.e., film formation temperature (FFT) should be higher than the Tg value), and an increase in the temperature difference between FFT and Tg value promotes the deformation capacity of the colloids and the polymer matrix continuity. The DSC thermograms of neat pBM, A-LNP-2.5-pBM, and A-LNP-4.0-pBM latex colloids showed only one strong and clear thermal transition, suggesting the thermal dynamic compatibility between A-LNPs and pBM without phase separation. It should be noted here that, when compared with the Tg of A-LNPs ranging from 77 to 48 °C (Figure S3a, Supporting Information) and the Tg of random pBM copolymer at 13 °C, the shift of Tg to the direction of lower temperature reveals the existence of an interpenetrating polymer network in the A-LNP-pBM latex, which is of importance for tough latex film applications. This observation is also consistent with the results reported by Xie et al.[50]

It is known that the Tg is highly dependent on the probing parameters. Therefore, in order to precisely compare the Tgs of various latex films in this work, Tg was also determined by temperature sweep experiment using dynamic mechanical analysis (DMA) under oscillation mode. At low temperatures (0–15 °C), neat pBM and A-LNP-pBM films exhibited a relaxation process corresponding to the glass-rubber transition of the pBM phase, as indicated by a stepwise decrease in extensional storage modulus (E′) and a peak in extensional loss modulus(E″), as shown in Figure 4c. It was found that the Tg, identified by the peak of E″, was almost identical to the Tg delineated from the DSC thermograms. Further heating resulted in a sharp drop in E′ of neat pBM until reaching a rubbery plateau starting from around 35 °C, whereas the rubbery plateau for A-LNP-pBM films was not obvious up to 50 °C. It is also known that E′ above Tg is a sensitive function of the polymer network architecture. Compared with neat pBM polymer, the viscoelastic behavior (i.e., the differences between E′ and E″) of A-LNP-pBM films exhibited lower dependence on temperature for a significant temperature range (20–35 °C). Importantly, the A-LNP-2.5-pBM and A-LNP-4.0-pBM films also exhibited higher E′ values

than the neat pBM films at room temperature, specifically, $E'_{A\text{-}LNP\text{-}4.0\text{-}pBM} > E'_{A\text{-}LNP\text{-}2.5\text{-}pBM} > E'_{pBM}$. The accumulated insight on the thermal-mechanical properties of latex films supports us to conclude that the core–shell emulsion polymerization using A-LNPs as the structural template can increase the mechanical stiffness of a pBM polymer matrix. It should be pointed out that the extensional modulus of A-LNP-1.5-pBM film could not be measured accurately during DMA temperature ramping (0–50 °C) measurement since its thermal transition had already occurred below the used temperature range.

To further rationalize the observed behaviors in thermal and mechanical properties, the morphology of the A-LNPs-based latex films was investigated with AFM, SEM, and X-ray diffraction (XRD)/SAXS (**Figure 5**). Compared with the topographical image of neat pBM latex film and its corresponding stiffness modulus distributions, the A-LNP-1.5-pBM latex film exhibited a slight phase separation (Figure 5a–d). The core–shell boundary of the A-LNP-2.5-pBM latex colloids seems to deform and forms a stiff honeycomb-like polymer matrix during the film formation, ascribed to the core-initiated covalent polymerization and the polymer chain coalescence (Figure 5e,f, see the zoomed in AFM image in Figure 5f). In addition, the coalescence on core–shell boundaries was more pronounced in the A-LNP-4.0-pBM film (Figure 5g,h, see the zoomed in AFM image in Figure 5h). Importantly, this honeycomb-like percolating structure, which contains a stiff and elastic phase together with a soft dispersed phase distributed throughout it, has been reported to enable surface-crosslinked acrylic colloids to form adhesive film with viscoelastic behavior at small strains and elastic behavior at large strains.[51] These results confirm that the tunability of the spherical core in terms of the abundance of polymerization-active anchors and their flexibility (e.g., Tg) indeed affects the deformability of latex colloids and the coalescence of core–shell boundary and, thus, the morphology of the latex films. The SEM cross-sectional morphology of the fabricated A-LNP-pBM films as shown in Figure 5k,l clearly indicates that the nanospheres were retained not only on the film surface but also embedded in the polymer matrix during latex colloids coalescence and final film formation.

The ultrastructure of the latex films was further investigated in terms of the crystallinity/ordering on molecular scale by XRD measurements. It was found that all pBM films, including the A-LNP-pBM ones, had a clear amorphous background with two broad diffraction peaks in an X-ray scattering angle range of $2\theta = 5°–30°$ (Figure 5m), which were due to the ordered packing of pBM polymer chains. Moreover, the most significant difference between pBM and A-LNP-pBM in the XRD profile is that only the ordered packing of side and main chains of poly(butyl acrylate) (pBA) were delineated for A-LNP-1.5-pBM film at $2\theta = 7°$ and 19°, respectively.[52] It should be noted here that the XRD pattern of the A-LNP-2.5-pBM and A-LNP-4.0-pBM latex films shows a distinct and sharp diffraction peak at $2\theta = 2.5°$, which indicates that the core–shell emulsion polymerization using A-LNPs as a structural template induced the formation of periodic mesostructures, typically confirming the presence of long-range hexagonal order with a 3.5 nm domain spacing.[53] Subsequently, the latex films were quantitatively evaluated in terms of the interpenetration degree of near-surface polymer chains on latex colloids using SAXS analysis. It should be noted here that the emulsion polymerization of pBM was initiated by the persulfate initiator and, thus, the negatively-charged groups, that is, sulfonate ions, were anchored at the colloidal surface.[26,54] In this scenario, the characteristic size of the interfacial domain boundaries (d_{inter}) between latex colloids was calculated based on the electron-density variation resulting from the spatial distribution of sulfate-terminated pBM polymer chains on latex colloids surfaces.[26,55] The plots of $[\ln q^4 I(q)]$ as a function of q^2 for the pBM and A-LNP-pBM films are displayed in Figure 5n, wherein the slope of the straight line fitted according to Porod's law affords the d_{inter} as listed in **Table 2** (Equation S1, Supporting Information). Noteworthy, a positive deviation was observed in the Porod region, indicating the formation of a well-defined and sharp domain boundary due to the diffusion of polymers in entangled melts upon thermal drying and annealing.[56] In latex films, average d_{inter} decreased in the order A-LNP-4.0-pBM (1.01 nm) > A-LNP-2.5-pBM (0.85 nm) > pBM (0.80 nm) > A-LNP-1.5-pBM (0.52 nm). This suggests that only the A-LNP-pBM latex colloids with uniform core–shell morphology can exhibit better polymer chain diffusivity than that of the neat pBM. In addition, the degree of interpenetration between pBM polymer shell increased with increasing the surface functionality of A-LNP core, especially when the A-LNP-2.5-pBM and A-LNP-4.0-pBM latex films were compared. It may be due to the fact that high molar mass of A-LNP-2.5-pBM polymer with a longer chain length than A-LNP-4.0-pBM exhibited pronounced entanglement rather than further interpenetration at the colloidal surface (Table S5 and Figure S8, Supporting Information). Compared with the neat pBM, restricted interpenetration of polymer chains at the near-surface of A-LNP-1.5-pBM latex colloids may be attributed to the phase separation of pBA and pBM. Poly(methyl methacrylate) (pMMA) was the dominant component of the pBM polymer shell of A-LNP-1.5-pBM, while the pBA oligomers were distributed in the polymer matrix, as is evident from the rather more BA extracts compared with MMA (Figure S6, Supporting Information) and two Tgs (e.g., –12 and 167 °C) delineated from its DSC thermogram (Figure 4b). Similar to previous studies,[26,55] the space distance of deformed latex colloids in pBM latex films can be investigated by SAXS profile. The SAXS pattern of A-LNP-1.5-pBM film exhibits a broad shoulder at $q = 0.25$ nm^{-1} (Figure S9, Supporting Information), corresponding to ≈25 nm center-to-center distance between the colloids, while this is not applicable for pBM, A-LNP-2.5-pBM, and A-LNP-4.0-pBM films in the q range of $q = 0.05–1.0$ nm^{-1}. This indicates that A-LNP-1.5-pBM colloids are highly deformed and packed in an ordered manner in the latex film, even though the polymer chain interpenetration is not significant. The absence of nanospheres in the SEM cross-sectional morphology of A-LNP-1.5-pBM confirmed its high deformability (Figure 5j). Above all, the results of morphology investigations from molecular to microscales emphasize the significance of a uniform core–shell nanostructure with strongly associated acrylate shell and defined polymer composition in achieving well-ordered re-arrangement and interpenetration between latex colloids during latex film formation.

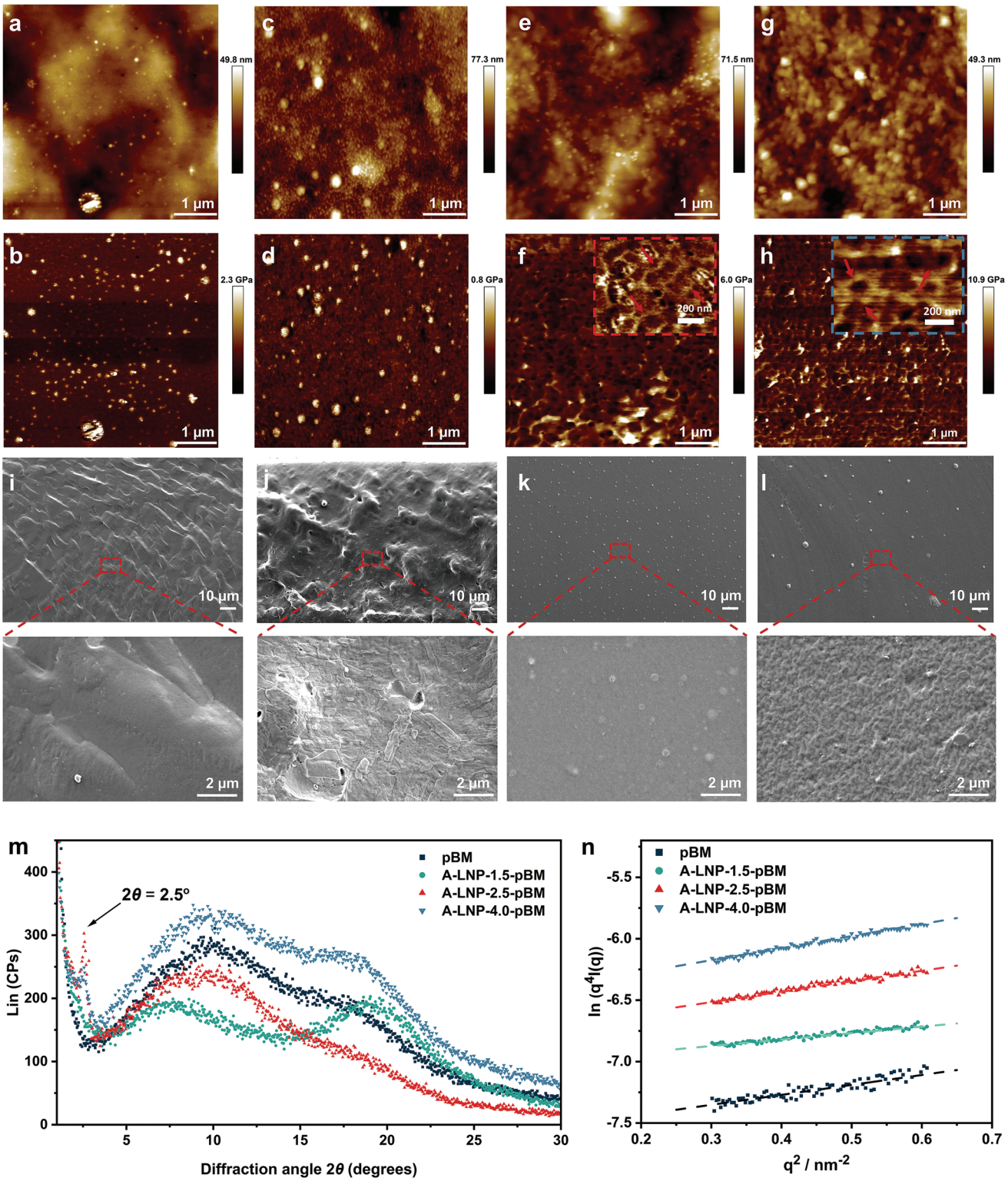

Figure 5. Ultrastructure of pBM and A-LNP-pBM latex films. AFM height images and its corresponding stiffness modulus distributions for a,b) neat pBM, c,d) A-LNP-1.5-pBM, e,f) A-LNP-2.5-pBM, and g,h) A-LNP-4.0-pBM films, respectively. The insets in (f) and (h) are the zoomed in images of the corresponding AFM images showing the honeycomb-like percolating structure. SEM images showing the cross-sectional morphology and nanostructure in i) neat pBM, j) A-LNP-1.5-pBM, k) A-LNP-2.5-pBM, and l) A-LNP-4.0-pBM films. m) XRD patterns of the latex films. n) Plots of $\ln[q^4 I(q)]$ as a function of q^2 for the latex films. The q in (n) was the scattering vector in SAXS measurement.

Table 2. The interfacial domain boundary size in the A-LNP-pBM latex films, including pBM film.

Films	d_{inter} [nm]
pBM	0.80 ± 0.02[a)]
A-LNP-1.5-pBM	0.52 ± 0.01
A-LNP-2.5-pBM	0.85 ± 0.01
A-LNP-4.0-pBM	1.01 ± 0.01

[a)]The standard deviations reflect the Porod's law fitting error from [ln$q$ ^{4}I(q)] as a function of q^2.

2.5. Mechanical Characteristics of A-LNP-pBM Latex Films

The mechanical properties of the latex films were evaluated by tensile tests. As noted in **Figure 6**a,b, the pBM latex films, including those integrated with A-LNPs, were stretchable and the films could recover automatically to their initial shapes and dimensions after the tensile load was removed, with the exception of the A-LNP-1.5-pBM film. The tensile stress of the A-LNP-1.5-pBM sample decreased beyond 160% elongation (Figure 6a), and "necking" was observed (Figure 6b). It can be inferred that the high deformability of the A-LNP-1.5-pBM colloids and their weak polymer chain interpenetration enable the film of superelongation, but with low tensile stress. In addition, the pBA (i.e., oligomers) in A-LNP-1.5-pBM latex film may serve as a plasticizer to further provide the film with a plastic profile. The effect of surface functionality of A-LNPs on the mechanical properties (e.g., stiffness, strength, and ductility) was evaluated. The elastic modulus (Figure 6c) and engineering stress (Figure 6d) of the A-LNP-pBM films increased with increasing surface functionality of A-LNPs and reached a maximum value of 78.0 MPa and 10.1 MPa at A-LNP-4.0-pBM, respectively. On the other hand, the elongation ratio of the A-LNP-pBM latex films decreased from 27.8 to 2.9 times their original lengths with increasing surface functionality of A-LNPs from 0.57 to 1.23 mmol g^{-1} (Figure 6e). Similarly, the surface-functionality-dependent interpenetration behavior between the A-LNP-pBM

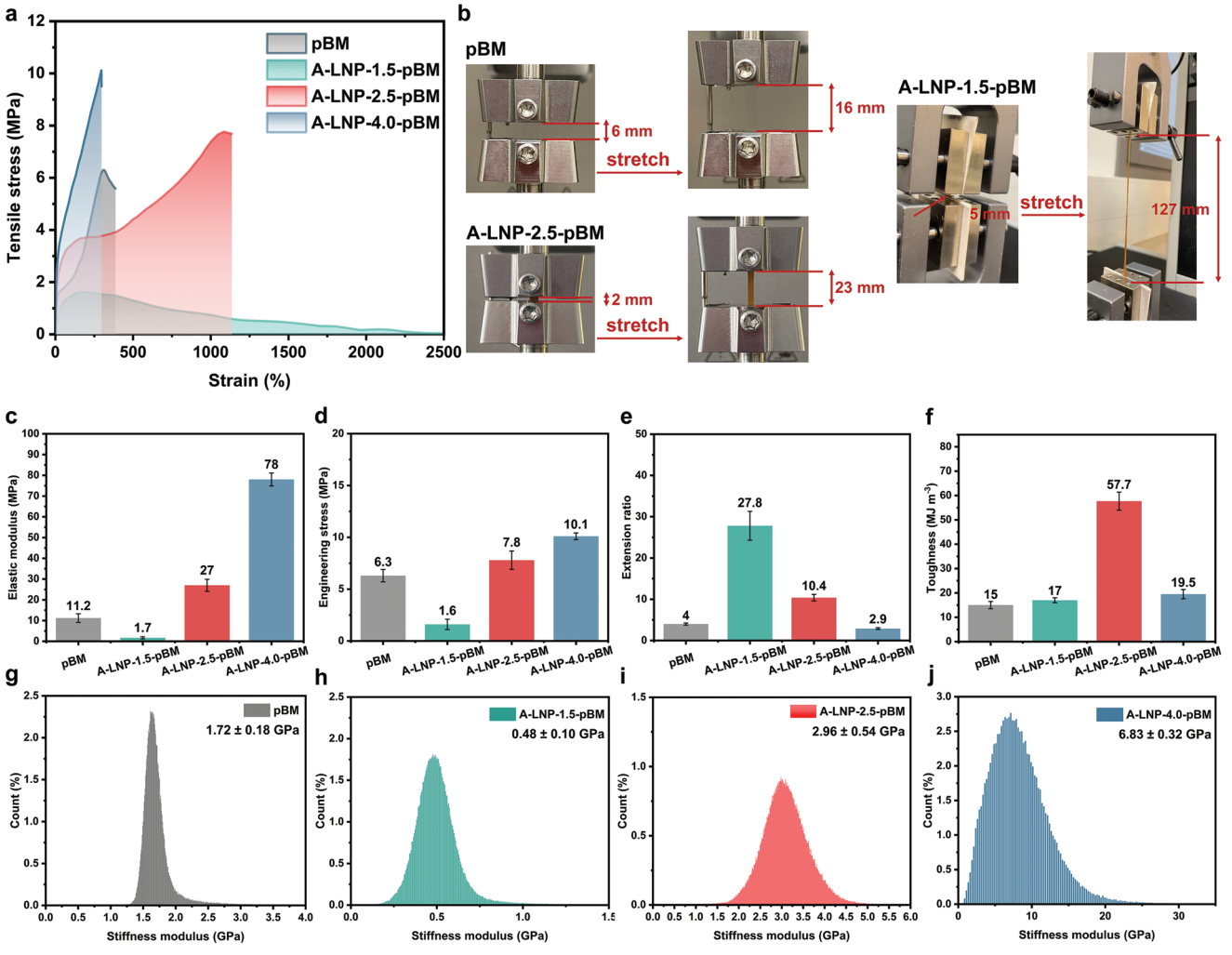

Figure 6. Mechanical properties of the latex films. a) Typical stress–strain curves of the latex films during tensile testing. b) The pBM, A-LNP-1.5-pBM, and A-LNP-2.5-pBM latex films were elongated to 3, 25, 11 times their initial lengths, respectively. c–f) Elastic modulus, engineering stress, extension ratio, and toughness versus surface functionality of A-LNPs for latex films. g–j) Histograms of stiffness modulus distribution as determined by AFM in PF-QNM mode using the Derjaguin–Muller–Toporov model.

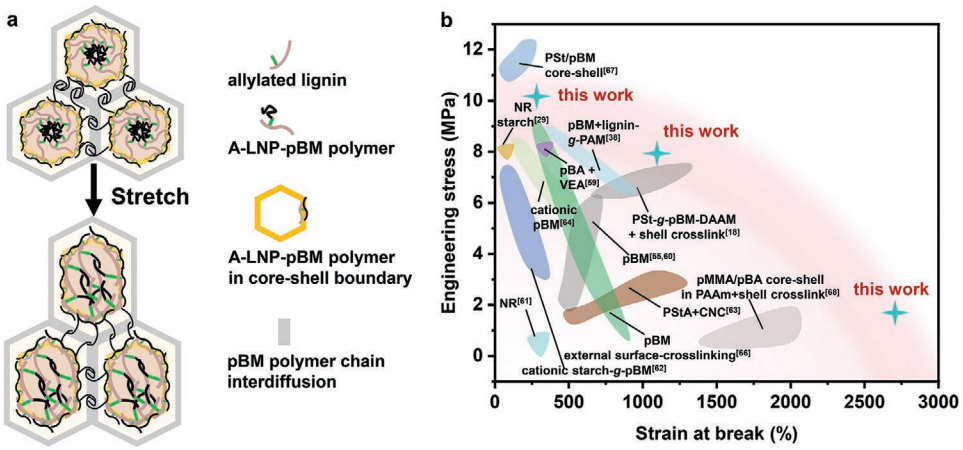

Figure 7. a) Schematic illustration of the toughness mechanism of A-LNP-pBM latex films during tensile deformation. b) Comparison of stress–strain at break of as-prepared A-LNP-pBM latex films with previous pBM composites films and a wide range of other latex films.

colloids turned out to be of high relevance for the mechanical properties of the films. The elastic modulus and tensile strength increased as the d_{inter} increased, while the ductility decreased. These results imply that pronounced latex colloids deformation and interdiffusion of polymer chains, as indicated by higher d_{inter} values, are key parameters for achieving exceptional mechanical properties. The trends of interpenetration degree of polymer chains directly correlated with the tensile strength of the latex films are in agreement with the results of film formation from PSt latex colloids reported in the literature.[57]

To further study the relationship between the ultrastructure of A-LNP-pBM latex films and their mechanical properties, the toughness, that is, the energy of mechanical deformation per unit volume prior to fracture, is compared in Figure 6f. The toughness value of the neat pBM film was 15.0 MJ m^{-3}, which is similar to that reported in the literature for latex film with the same BA and MMA compositions.[55] It can be seen that the pBM film exhibited high toughness when integrated with A-LNP-pBM core–shell latex colloids. In particular, the A-LNP-2.5-pBM film delineated both strong and ductile profiles, where the toughness value significantly increased to 57.7 MJ m^{-3} compared to the neat pBM film. We confer that the high toughness of the A-LNP-2.5-pBM latex film could be attributed to three factors. First, the A-LNPs, BA, and MMA have covalent interactions with each other, which enabled A-LNPs to interpenetrate the pBM polymer matrix and reinforce the latex film. The formation of a honeycomb-like core–shell boundary matrix together with a core-stimulated periodic mesostructure during the film-forming process also supports the above-mentioned hypothesis, as delineated by AFM in Figure 5f and XRD measurement in Figure 5m. Second, the pBM polymers can be well dispersed in the A-LNP-pBM matrix, which is evident from the difference in SEM cross-sectional morphology of A-LNP-2.5-pBM (Figure 5i) and pBM (Figure 5k) films, wherein more even and nanosphere-embedded nanostructures are depicted in A-LNP-2.5-pBM film. Furthermore, the polymerization fashion of pBM polymers interpenetrating A-LNPs and spatially surrounding the A-LNPs through polymerization-active anchors can dissipate energy during large deformations because of the nano-confinement effect of covalently associated A-LNP-pBM cores, as illustrated in **Figure 7**a. More specifically, as the latex film is deformed, relatively short pBM polymer chains across the A-LNPs can be fractured or disentangled to dissipate mechanical energy while rather long pBM polymers that assembled on the A-LNP cores can still arrange in core–shell boundary and bridge between the latex colloids to maintain high elasticity of the latex film.[58] Nevertheless, highly crosslinked nanospheres, wherein the average chain length for the nanosphere is short, should be easily fractured.[24] This notion is supported by the low toughness of A-LNP-4.0-pBM film (19.5 MJ m^{-3}). Third, the fracture at the interface between A-LNP-pBM latex colloids may be inhibited by the increased contact area since A-LNP-2.5-pBM nanospheres have smaller particle size than pBM ones.[55] Another key engineering parameter of thin film is its surface mechanical properties. As noted in Figure 6g–j, the surface stiffness modulus as determined by AFM in Peakforce Quantitative Nanomechanical Mapping (PF-QNM) mode increased in the order A-LNP-1.5-pBM (0.48 GPa) < pBM (1.72 GPa) < A-LNP-2.5-pBM (2.96 GPa) < A-LNP-4.0-pBM (6.83 GPa), which is well consistent with the tensile test results.

The toughness of latex films has been highlighted as a desired property for use as coatings and binders in textile, papermaking, and leather industries.[59,60] Hereby, we compared and discussed our approach to fabricate tough bio-latex films with other existing approaches in the literature (Figure 7b). The stress–strain at break reported here exceeds those reported for natural rubber (NR) and other novel bio-latexes reinforced with starch,[29,61,62] cellulose nanocrystals (CNC),[63,64] and bio-based vanillin-eugenol-acrylate (VEA).[59] Most commonly, in order to obtain toughness, external surface-crosslinking rather than internal crosslinking is in need to govern the interdiffusion of polymer chain and the full coalescence of colloids as well as the strength of individual colloids.[65] For instance, keto-hydrazide acrylic emulsion crosslinking chemistry, such as using diacetone acrylamide (DAAm) with adipic acid dihydrazide (ADH) and (2-acetoacetoxy)ethyl methacrylate (AAEM) with hexamethylenediamine (HMDA), enabled the occurrence of post-crosslinking during film formation process to improve the toughness of pBM and poly(styrene-acrylate) (PStA) latex films.[18,66] Using core–shell structured polyacrylic modifiers

and in combination with surface-crosslinking had also been reported to toughen PStA latex films and polyacrylamide (PAAm) hydrogels.[67,68] Another way to prepare tough bio-latex films is by fabricating bio-derived macro-CT agents for RAFT polymerization. Recently, Xu et al. reported the preparation of pBM bio-latex by RAFT method using lignin-xanthate-graft-polyacrylamide (lignin-*g*-PAM) as a macro-CT agent.[38] However, the toughness enhancement of latex films was limited to a 5 wt% lignin loading relative to the total weight of acrylate monomers, whereas a 10 wt% lignin content provided the films with only strong but not ductile feature. Compared with these studies, the super-toughness of pBM latex films reported in this work and the tunability of mechanical properties, ranging from stiff to ductile thermoplastics and further to ultrastretchable elastomers, are achieved by tailoring the surface-functionality of A-LNPs. The surface-active A-LNPs core can facilitate the formation of a uniform pBM shell on it and stimulate the formation of an interpenetrating A-LNP-pBM polymer network together with a honeycomb-like percolating structure to toughen the latex films. Under the principles of sustainability, our approach enables high lignin content (20 wt% of total BA and MMA weights) and mitigates the use of petroleum-based crosslinkers, such as DAAm–ADH and AAEM–HMDA. In addition, A-LNP-pBM latex films were comparable to those of the PStA-based core–shell latex films in terms of elongation ratio and engineering stress. We strongly believe that the as-proposed synthetic route of integrating nano-lignin in a core–shell latex film with such a high efficiency provides a sustainable but viable strategy to address the bio-based alternatives demanded by petroleum-based latex products.

3. Conclusion

We have shown the allylated lignin conveniently forms lignin nanospheres via self-assembly in a purifying dialysis process, and this surface-activated nano-lignin can then be successfully integrated as the hard core in a seeded free-radical emulsion polymerization of BA and MMA monomers to fabricate core–shell latex colloids. During the emulsion polymerization in aqueous medium, allyl aryl ether distributed on A-LNPs serves as a polymerization-modulating anchor to facilitate the covalent interpenetration of A-LNP core with the shell of acrylate polymer, which in the end addresses the development bottleneck of insufficient toughness of conventional bio-latex films without using any plasticizers. The abundance content of allyl-terminated anchors on A-LNPs largely dominates the size, polymeric flexibility, and surface hydrophobicity of the lignin nanospheres. All these factors define the accessibility of polymerization-active anchors in terms of modulating the interfacial recognition of monomers. When forming a thermally annealed latex film, the core–shell nanostructure specifics in latex colloids do make differences in the resulting film morphology and consequently in its mechanical characteristics. In terms of toughening the bio-latex film, the optimized one exhibited excellent mechanical properties (e.g., engineering stress ≈8 MPa and toughness value ≈58 MJ m^{-3}) while possessing low Tg values (≈8–13 °C). Images obtained with PF-QNM AFM and SEM, as well as SAXS patterns, revealed that the bio-latex films possessed a higher toughness than the neat latex film due to flattened domains with distinct core–shell boundaries maintained after latex colloids coalescence when thermally annealed above Tg. We anticipate that this approach can be extended to the design of acrylate compositions that contain diverse functional monomers.

4. Experimental Section

Materials: The birch alkaline lignin used in this work was provided by CH-Bioforce Oy (Finland). The detailed lignin manufacturing and purification processes are available in the Supporting Information. The birch-*i*-PrOH lignin was prepared following the protocol reported in the previous work and was well characterized in terms of purity, molar mass characteristics, and structural features.[69,70] The carbohydrate content in birch-*i*-PrOH was 0.24 wt%, hydrolyzed using acid methanolysis method and quantified by gas chromatography. The number-averaged molar mass and weight-averaged molar mass of birch-*i*-PrOH determined by size-exclusion chromatography (SEC) were 2850 and 3700 g mol^{-1}, respectively. Allyl glycidyl ether, MMA, BA, SDS, and APS were purchased from Sigma-Aldrich and used as received if not stated otherwise. MilliQ-water (18.2 MΩ cm^{-1}) was used.

A-LNPs Dispersion Preparation: Lignin (250 mg birch-*i*-PrOH, 4.71 mmol g^{-1} hydroxyl groups) was introduced to a two-necked round-bottom flask containing 10 mL of sodium hydroxide (NaOH, 0.2 g, 0.5 M) aqueous solution under agitation. The flask was equipped with a reflux condenser and immersed into an oil bath preheated to 60 °C. Allyl glycidyl ether (135 mg, 1.18 mmol) was provided dropwise to the homogeneous lignin solution using a syringe through a septum in a nitrogen (N_2) atmosphere and the reaction was left to stir for 10 h. The reaction was terminated by cooling to ambient temperature. The reaction media was dialyzed against Milli-Q water using a 1000 Da dialysis membrane (Spectra/Por 7) to remove the unreacted reactants until the conductivity of the dialysis solution was close to Milli-Q water. Consequently, the A-LNP-1.0 dispersion was obtained. The same sample preparation procedure was carried out to obtain the A-LNP-1.5, A-LNP-2.5, and A-LNP-4.0 dispersions, while the content of allyl glycidyl ether was tuned to achieve different stoichiometric molar ratios to lignin hydroxyl groups (Table S1, Supporting Information).

A-LNP-pBM Latex Colloids and Film Fabrication: The core–shell A-LNP-pBM latex colloids were prepared by free-radical emulsion polymerization under the following conditions. The two-necked round-bottom flask containing 20 mL dispersion of A-LNP-2.5 (250 mg lignin) was deoxygenated by purging with N_2 for 20 min and was thereafter equipped with a condenser and immersed into an oil bath preheated to 80 °C. Then, SDS (12.5 mg, 0.04 mmol) and APS (12.5 mg, 0.05 mmol) were introduced to the dispersion in a N_2 atmosphere. Mixed acrylate monomers of BA (625 mg, 4.88 mmol) and MMA (625 mg, 6.24 mmol) with a total mass fivefold to the lignin were added dropwise with a peristaltic pump through the rubber septum sealed on the neck of the flask within 1 h, thus initializing the polymerization. The reaction was performed under 400 rpm stirring with continuous N_2 purging, and another portion of APS (12.5 mg, 0.05 mmol) was introduced to the reaction media at 4 h. The reaction was terminated at 6 h to obtain A-LNP-2.5-pBM latex by cooling to room temperature. This procedure was representative of all the polymerization conducted herein. Specifically, the pBM latex colloids were synthesized without lignin but following the same procedure as for A-LNP-2.5-pBM latex. The detailed experimental design of A-LNP-pBM latex colloids is listed in Table S6, Supporting Information. To prepare latex films, 6.5 g of pBM or A-LNP-pBM latex emulsion was loaded onto a plastic petri dish (surface area 20.4 cm^2) with a dry mass loading of 25–26 mg m^{-2}. Latex films with thickness of about 150 µm were obtained after drying and annealing at 50 °C for 18 h.

TEM: The morphology of A-LNPs and A-LNP-pBM latex colloids was characterized using a JEM-1400 PLUS microscope (JEOL Ltd., Japan)

in bright-field mode, and uranyl acetate staining was used for sample preparation of latex colloids (see details in Supporting Information).

HPLC: Quantitative BA and MMA monomer conversion kinetic curves were obtained from an HPLC (Agilent 1260 Infinity, USA) equipped with an ultraviolet diode array detector performed at 210 nm (see details on operating conditions in Supporting Information). The BA and MMA residues in latex emulsion were extracted with HPLC-grade methanol (MeOH) at a MeOH/H_2O volume ratio of 9:1 (v/v) at room temperature for 2 h prior to HPLC analysis.

NMR: All the NMR experiments were performed on an AVANCE III 500 MHz spectrometer (Bruker Ltd., Switzerland) equipped with a 5 mm Z-gradient Broadband Observe CryoProbe (see details on sample preparation in Supporting Information).

SEC: Molar mass determination was carried out by an SEC system (Agilent 1100/1200/1260 Series, USA) equipped with a multi-angle light scattering detector (Wyatt Technology DAWN 8 ambient) and a differential refractive index concentration detector (Wyatt Technology Optilab High Concentration), following the protocol reported in a previous publication.[71] This method allows the detection of absolute molar mass compared to universal calibrations using specific standards. The resulting latex emulsions were purified by two cycles of centrifugation and re-dispersion, replacing each decanted supernatant with Milli-Q water followed by freeze-drying. The freeze-dried latex samples were dissolved in DMSO eluent containing 0.05 M lithium bromide to 10 mg mL^{-1} overnight before SEC analysis.

Surface Tension: The surface tension of A-LNP solution (1.0 mg mL^{-1}, pH 13.3) against air was measured with a force tensiometer-K100 (Krüss, Germany) using a Wilhelmy plate at 25 °C.

XPS: A Nexsa XPS instrument (ThermoFisher Scientific, USA) operating with monochromated Al Kα X-ray sources was used to analyze the chemical composition in the near-surface of A-LNPs (see details on spectral deconvolution in Supporting Information).

DSC: Thermal properties of A-LNPs and A-LNP-pBM latex colloids were evaluated by DSC 25 (TA Instrument, USA) under N_2 atmosphere (see details on temperature program in Supporting Information).

AFM: All the AFM measurements were carried out with a MultiMode 8 AFM (Bruker, Santa Barbara, CA) equipped with a Nanoscope V controller in ambient air. SCANASYST-AIR probes (Bruker, k: 0.4 N m^{-1}, f_0: 70 kHz) were used for the PF-QNM AFM measurements of latex films. The spring constant was calibrated at 33–35 N m^{-1} by using the Sader method. A clean fused silica substrate (Bruker, Santa Barbara, CA) was used to calibrate the deflection sensitivity (32–34 nm V^{-1}) and a reference PSt film (Bruker, Santa Barbara, CA) with a Young's modulus of 2.7 GPa was used to calibrate the tip radius at a certain indentation depths, typically 2–3 nm. The used scan size was 5×5 μm^2 with a resolution of 1024×1024 pixels. The scanning speed was 1 Hz. Nanoscope Analysis (version 1.5, Bruker) was used for data analysis.

WCA: The static WCA of A-LNPs thin films absorbed on poly-L-lysine (PLL) pre-coated silicon wafer was measured with a KSV CAM200 instrument (KSV Instruments Ltd, Finland) using a sessile drop method (see details on sample preparation in Supporting Information). The high coverage of the A-LNPs on PLL-coated silicon wafer was confirmed by its AFM topographical feature using gold-coated silicon probes (NSG03 AFM probe, NT-MDT, Russia) (see details in Supporting Information).

TSI: The A-LNP-pBM emulsion stability was characterized by TURBISCAN^{LAB} analyzer (Formulaction, France) equipped with a pulsed near infrared light source ($\lambda = 880$ nm) and synchronous optical detectors at 25 °C.

DMA: Temperature ramp analysis was performed on A-LNP-pBM latex films using DMA (MCR 702 Multidrive, Anton Paar, Austria) to measure the dynamic extensional moduli as a function of temperature by applying a constant amplitude oscillation within the linear viscoelastic range (see details in Supporting Information).

SEM: A LEO 1530 Gemini SEM (Zeiss/LEO, Germany) with an accelerating voltage of 2.70 kV was used to analyze the cross-sectional morphology of latex films. The cross-section samples were prepared through a freeze-fracture method by first freezing the sample with liquid nitrogen. The samples were sputter-coated with platinum prior to SEM imaging.

XRD: XRD of latex films was performed on a Bruker AXS D8 Discover diffractometer (Bruker AXS, Germany) with CuKα radiation ($\lambda = 1.54184$ Å) under 40 kV accelerating voltage and 40 mA emission current. The diffraction angle 2θ was from 0.5 to 30° with a step size of 0.04° (2θ).

SAXS: The SAXS analysis was performed on latex films in a perpendicular transmission geometry at 25 °C under vacuum using synchrotron X-rays derived from the beamline BL03XU of Spring-8 (Japan). High-resolution mode (0.4×0.4 mm^2 beam size) and sample-to-detector distances 1100 mm were applied for SAXS measurements. More specifically, the SAXS measurement was carried out using a parallel beam focused and monochromized by a multilayer mirror. The instrument effect on diffraction peak broadening, as measured by the full width at half maximum of lanthanum hexaboride standard sample, was not more than 0.3 nm^{-1} in q-range, which has no effect on the SAXS data (see details on Porod's law fitting in Supporting Information).

Tensile Tests: The mechanical properties of the latex films were measured using a Lloyd Ir30 universal testing machine (Lloyd Instruments Ltd, UK) equipped with a 250 N loaded cell at a strain rate of 20 mm min^{-1} (see details on sample preparation in Supporting Information).

Supporting Information

Supporting Information is available from the Wiley Online Library or from the author.

Acknowledgements

L.W. and Q.W. would like to acknowledge the financial support from the China Scholarship Council (student ID 201804910639 for L.W. and student ID 201907960002 for Q.W.) for their doctoral study at ÅAU, Finland. L.W. and C.X. would like to acknowledge funding from Business Finland Project (43674/31/2020). X.W. would like to thank Academy of Finland (333158) as well as Jane and Aatos Erkko Foundation for their funds for her research at ÅAU. E.R. and J.P. acknowledge Jane and Aatos Erkko Foundation for providing funding for the work. Electron microscopy samples were processed and analyzed in the Electron Microscopy Laboratory, Institute of Biomedicine, University of Turku, which received financial support from Biocenter Finland. The authors acknowledge the provision of facilities and technical support by Aalto University at OtaNano—Nanomicroscopy Center (Aalto-NMC).

Conflict of Interest

The authors declare no conflict of interest.

Data Availability Statement

The data that support the findings of this study are available from the corresponding author upon reasonable request.

Keywords

acrylics, core–shell latex colloids, free-radical emulsion polymerization, lignin nanoparticles, toughness

Received: November 14, 2022
Revised: January 2, 2023
Published online: March 15, 2023

[1] Q. Chen, S. C. Bae, S. Granick, *Nature* **2011**, *469*, 381.
[2] L. F. Francis, J. C. Grunlan, J. Sun, W. W. Gerberich, *Colloids Surf., A* **2007**, *311*, 48.
[3] P. Vandervorst, C. H. Lei, Y. Lin, O. Dupont, A. B. Dalton, Y. P. Sun, J. K. Keddie, *Prog. Org. Coat.* **2006**, *57*, 91.
[4] W. Liu, M. Kappl, H. J. Butt, *ACS Nano* **2019**, *13*, 13949.
[5] Y. Hu, D. Yang, S. Huang, *ACS Omega* **2019**, *4*, 18771.
[6] A. P. Richez, H. N. Yow, S. Biggs, O. J. Cayre, *Prog. Polym. Sci.* **2013**, *38*, 897.
[7] J. Engström, C. J. Brett, V. Körstgens, P. Müller-Buschbaum, W. Ohm, E. Malmström, S. V. Roth, *Adv. Funct. Mater.* **2020**, *30*, 1907720.
[8] M. C. D. Carter, L. Chen, R. S. Moglia, P. Luo, T. S. Ratani, M. Janco, J. Gu, J. N. Ngunjiri, W. Gao, C. L. Jackson, R. C. Even, *ACS Appl. Polym. Mater.* **2019**, *1*, 3185.
[9] E. B. Mock, H. D. Bruyn, B. S. Hawkett, R. G. Gilbert, C. F. Zukoski, *Langmuir* **2006**, *22*, 4037.
[10] D. R. Stutman, A. Klein, M. S. El-Aasser, J. W. Vanderhoff, *Ind. Eng. Chem. Prod. Res. Dev.* **1985**, *24*, 404.
[11] W. Hou, W. Zhong, H. Zhao, *Macromolecules* **2021**, *54*, 2617.
[12] Q. Yong, J. Xu, L. Wang, T. Tirri, H. Gao, Y. Liao, M. Toivakka, C. Xu, *Carbohydr. Polym.* **2022**, *291*, 119565.
[13] J. G. Tsavalas, J. W. Gooch, F. J. Schork, *J. Appl. Polym. Sci.* **2000**, *75*, 916.
[14] Y. Lin, A. K. Tripathi, J. G. Tsavalas, *ACS Appl. Polym. Mater.* **2022**, *4*, 313.
[15] X. Zhang, J. Sun, Y. Chen, Q. Chen, L. Bai, J. Gu, Z. Li, *ACS Appl. Polym. Mater.* **2022**, *4*, 1276.
[16] J. Li, Y. Shao, C. Zhang, H. Duan, D. Qi, *ACS Appl. Polym. Mater.* **2022**, *4*, 7115.
[17] P. A. Lovell, F. J. Schork, *Biomacromolecules* **2020**, *21*, 4396.
[18] K. Xu, K. Putera, M. Wawryk, J. Wan, B. Peng, M. M. Banaszak Holl, A. F. Patti, S. H. Thang, *Macromolecules* **2022**, *55*, 5301.
[19] X. You, X. Wang, H. J. Zhang, K. Cui, A. Zhang, L. Wang, C. Yadav, X. Li, *ACS Appl. Mater. Interfaces* **2020**, *12*, 39892.
[20] Y. Shi, C. Liu, L. Liu, L. Fu, B. Yu, Y. Lv, F. Yang, P. Song, *Chem. Eng. J.* **2019**, *378*, 122267.
[21] M. Ma, H. T. Davis, L. E. Scriven, *Prog. Org. Coat.* **2005**, *52*, 46.
[22] C. C. Roberts, L. F. Francis, *J. Coat. Technol. Res.* **2013**, *10*, 441.
[23] J. W. Taylor, A. M. Winnik, *JCT Res.* **2004**, *1*, 163.
[24] S. Hiroshige, T. Kureha, D. Aoki, J. Sawada, D. Aoki, T. Takata, D. Suzuki, *Eur. J. Chem.* **2017**, *23*, 8405.
[25] D. Aoki, S. Uchida, K. Nakazono, Y. Koyama, T. Takata, *ACS Macro Lett.* **2013**, *2*, 461.
[26] T. Kureha, S. Hiroshige, D. Suzuki, J. Sawada, D. Aoki, T. Takata, M. Shibayama, *Langmuir* **2020**, *36*, 4855.
[27] S. H. Chen, A. J. Souna, S. J. Stranick, M. Jhalaria, S. K. Kumar, C. L. Soles, E. P. Chan, *Soft Matter* **2022**, *18*, 256.
[28] A. Romo-Uribe, *Macromol. Mater. Eng.* **2021**, *306*, 2000591.
[29] N. Romo Leksawasdi, T. Chaiyaso, P. Rachtanapun, S. Thanakkasaranee, P. Jantrawut, W. Ruksiriwanich, P. Seesuriyachan, Y. Phimolsiripol, C. Techapun, S. R. Sommano, T. Ougizawa, K. Jantanasakulwong, *Sci. Rep.* **2021**, *11*, 19250.
[30] A. Nasiri, J. Wearing, M. A. Dubé, *Int. J. Adhes. Adhes.* **2020**, *100*, 102598.
[31] L. Wang, Q. Wang, A. Slita, O. Backman, Z. Gounani, E. Rosqvist, J. Peltonen, S. Willför, C. Xu, J. M. Rosenholm, X. Wang, *Green Chem.* **2022**, *24*, 2129.
[32] M. Morsali, A. Moreno, A. Loukovitou, I. Pylypchuk, M. H. Sipponen, *Biomacromolecules* **2022**, *23*, 4597.
[33] E. Kimiaei, M. Farooq, R. Grande, K. Meinander, M. Österberg, *Adv. Mater. Interfaces* **2022**, *9*, 2270152.
[34] A. Moreno, M. Morsali, J. Liu, M. H. Sipponen, *Green Chem.* **2021**, *23*, 3001.
[35] D. Gan, W. Xing, L. Jiang, J. Fang, C. Zhao, F. Ren, L. Fang, K. Wang, X. Lu, *Nat. Commun.* **2019**, *10*, 1487.
[36] Q. Cao, Q. Wu, L. Dai, C. Li, Y. Zhong, F. Yu, R. Li, C. Si, *Ind. Crops Prod.* **2021**, *172*, 114012.
[37] Q. Cao, Q. Wu, L. Dai, X. Shen, C. Si, *Green Chem.* **2021**, *23*, 2329.
[38] Y. Xu, N. Li, G. Wang, C. Wang, F. Chu, *Polymers* **2021**, *13*, 968.
[39] N. Toncheva-Moncheva, M. Dangalov, N. G. Vassilev, C. P. Novakov, *RSC Adv.* **2020**, *10*, 25214.
[40] E. A. Baroncini, J. F. Stanzione, *Int. J. Biol. Macromol.* **2018**, *113*, 1041.
[41] H. Yang, A. Sun, C. Chai, W. Huang, X. Xue, J. Chen, B. Jiang, *Polymer* **2017**, *121*, 256.
[42] J. T. Miao, L. Yuan, Q. Guan, G. Liang, A. Gu, *ACS Sustainable Chem. Eng.* **2018**, *6*, 7902.
[43] S. Gong, H. Chen, X. Zhou, S. Gunasekaran, *R. Soc. Open Sci.* **2017**, *4*, 170844.
[44] M. Rahman, A. Ali, E. Sjöholm, S. Soindinsalo, C. E. Wilén, K. K. Bansal, J. M. Rosenholm, *Pharmaceutics* **2022**, *14*, 798.
[45] Y. Qiang, S. S. Pande, D. Lee, K. T. Turner, *ACS Nano* **2022**, *16*, 6372.
[46] I. V. Pylypchuk, P. A. Lindén, M. E. Lindström, O. Sevastyanova, *ACS Sustainable Chem. Eng.* **2020**, *8*, 13805.
[47] M. Hubbe, R. Alén, M. Paleologou, M. Kannangara, *BioResources* **2019**, *14*, 2300.
[48] A. S. Brar, S. Kaur, *Polym. J.* **2005**, *37*, 316.
[49] S. Chandran, J. K. Basu, M. K. Mukhopadhyay, *J. Chem. Phys.* **2013**, *138*, 014902.
[50] R. Xie, A. R. Weisen, Y. Lee, M. A. Aplan, A. M. Fenton, A. E. Masucci, F. Kempe, M. Sommer, C. W. Pester, R. H. Colby, E. D. Gomez, *Nat. Commun.* **2020**, *11*, 893.
[51] F. Deplace, M. A. Rabjohns, T. Yamaguchi, A. B. Foster, C. Carelli, C. H. Lei, K. Ouzineb, J. L. Keddie, P. A. Lovell, C. Creton, *Soft Matter* **2009**, *5*, 1440.
[52] K. Matsuura, K. Kuboyama, T. Ougizawa, *J. Appl. Polym. Sci.* **2021**, *138*, 50268.
[53] S. Poppe, A. Lehmann, A. Scholte, M. Prehm, X. Zheng, G. Ungar, C. Tschierske, *Nat. Commun.* **2015**, *6*, 8637.
[54] Y. Wang, C. L. Zhao, M. A. Winnik, *J. Chem. Phys.* **1991**, *95*, 2143.
[55] S. Hiroshige, H. Minato, Y. Nishizawa, Y. Sasaki, T. Kureha, M. Shibayama, K. Uenishi, T. Takata, D. Suzuki, *Polym. J.* **2021**, *53*, 345.
[56] S. Vaishali Sethi, S. K. Mehta, A. K. Ganguli, S. Vaidya, *Phys. Chem. Chem. Phys.* **2019**, *21*, 336.
[57] J. N. Yoo, L. H. Sperling, C. J. Glinka, A. Klein, *Macromolecules* **1991**, *24*, 2868.
[58] X. Zhao, *Soft Matter* **2014**, *10*, 672.
[59] L. Zhang, J. Ma, B. Lyu, Y. Zhang, V. K. Thakur, C. Liu, *Green Chem.* **2021**, *23*, 7576.
[60] P. Neelambaram, A. Shankar, K. Sykam, D. B. R. Kumar, A. Chakrabarty, R. Narayan, *Prog. Org. Coat.* **2022**, *171*, 107011.
[61] S. Nooma, R. Magaraphan, *Polym. Bull.* **2019**, *76*, 3329.
[62] L. D. A. Rodrigues, L. M. Guerrini, M. P. Oliveira, *J. Therm. Anal. Calorim.* **2021**, *146*, 143.
[63] Y. He, M. Jiang, W. Hu, I. Ahmad, L. Gan, A. Pang, J. Huang, *J. Polym. Res.* **2022**, *29*, 399.
[64] E. Limousin, I. Rafaniello, T. Schäfer, N. Ballard, J. M. Asua, *Langmuir* **2020**, *36*, 2052.
[65] M. Li, W. Liu, Q. Zhang, S. Zhu, *ACS Appl. Mater. Interfaces* **2017**, *9*, 15156.
[66] J. Lesage de la Haye, M. Martin-Fabiani, M. Schulz, J. L. Keddie, F. D'Agosto, M. Lansalot, *Macromolecules* **2017**, *50*, 9315.
[67] L. Bai, S. Huan, X. Zhang, J. Gu, Z. Li, *Int. J. Adhes. Adhes.* **2016**, *70*, 152.

[68] X. Ren, C. Huang, L. Duan, B. Liu, L. Bu, S. Guan, J. Hou, H. Zhang, G. Gao, *Soft Matter* **2017**, *13*, 3352.
[69] L. Wang, L. Lagerquist, Y. Zhang, R. Koppolu, T. Tirri, I. Sulaeva, S. von Schoultz, L. Vähäsalo, A. Pranovich, T. Rosenau, P. C. Eklund, S. Willför, C. Xu, X. Wang, *ACS Sustainable Chem. Eng.* **2020**, *8*, 13517.
[70] L. Wang, L. Tan, L. Hu, X. Wang, R. Koppolu, T. Tirri, B. v. Bochove, P. Ihalainen, L. S. Seleenmary Sobhanadhas, J. V. Seppälä, S. Willför, M. Toivakka, C. Xu, *ACS Sustainable Chem. Eng.* **2021**, *9*, 8770.
[71] G. Zinovyev, I. Sulaeva, S. Podzimek, D. Rössner, I. Kilpeläinen, I. Sumerskii, T. Rosenau, A. Potthast, *ChemSusChem* **2018**, *11*, 3259.